

Calibration of Biophysical Models for tau-Protein Spreading in Alzheimer's Disease from PET-MRI

Klaudius Scheufele^{1,*}, Shashank Subramanian¹, and George Biros¹

¹Oden Institute, The University of Texas at Austin, Texas, USA

*kscheufele@austin.utexas.edu

ABSTRACT

Aggregates of misfolded tau proteins (or just “tau” for brevity) play a crucial role in the progression of Alzheimer's disease (AD) as they correlate with cell death and accelerated tissue atrophy. Longitudinal positron emission tomography (PET) is used to measure the extent of tau inclusions; and PET-based image biomarkers are a promising technology for AD diagnosis and prognosis. Here, we propose to combine an organ-scale biophysical mathematical model and longitudinal PET to extract characteristic growth patterns and spreading of tau. The biophysical model is a reaction-advection-diffusion partial differential equation (PDE) with only two unknown parameters representing the spreading (the diffusion part of the PDE) and growth of tau (the reaction part of the PDE). The advection term captures tissue atrophy and is obtained from diffeomorphic registration of longitudinal magnetic resonance imaging (MRI) scans. We describe the method, present a numerical scheme for the calibration of the growth and spreading parameters, perform a sensitivity study using synthetic data, and apply it to clinical scans from the ADNI dataset. Despite having only two parameters, the model can reconstruct clinical scans quite accurately.

Introduction

Alzheimer's disease is the sixth highest leading cause of death in the US (alz.org). Its complex evolution is thought to be closely related to the formation and spreading of abnormal proteinaceous assemblies in the nervous system. In particular, the misfolding of β -amyloid ($A\beta$) and tau proteins are believed to be key factors driving the progression of Alzheimer's¹⁻³. These corruptive templates incite a chain reaction of protein misfolding, by imposing their anomalous structure on benign molecules. Subsequent growth, fragmentation and further spreading of such toxic proteins hampers proper function of the nervous system, leads to accelerated tissue atrophy, necrosis, and ultimately causes death⁴⁻⁷.

Tau aggregates are primarily found in the axon bundle and rapidly spread along neuronal pathways to distant locations, but also invade the extracellular space⁸. Understanding the distinct spatiotemporal growth patterns and original seeding of corrupted protein templates is imperative in developing new treatment protocols and can reveal important complimentary information to aid diagnosis and overall efficacy of therapy. Longitudinal PET scans (using the F-AV-1451 tracer) can image tau spreading and lead to improved diagnosis and prognosis. Many groups are designing image-analysis algorithms for this purpose⁹⁻¹². Here we propose a complementary approach: We employ a PDE model of tau propagation and calibrate its parameters using longitudinal PET scans. *Our goal is to estimate such rates of amplification of misfolded tau-protein aggregates and the rate of fragmentation and migration thereof to distant parts of the brain.* Our hypothesis is that an informative *minimal* model can produce biomarkers, which can augment imaged-based approaches. Once calibrated, the current and future spatiotemporal spreading of tau can be quantified using our model.

Contributions. The novelty of our work can be summarized as follows:

1) We solve an inverse problem to estimate patient specific, characteristic growth parameters describing the spatiotemporal evolution of misfolded tau-protein throughout the brain based on longitudinal 3D tau-PET imaging of AD subjects. We model tau progression as reaction-diffusion-advection PDE which accounts for both, atrophy and tau propagation; atrophy is modeled using material transport with a velocity obtained from diffeomorphic image registration, and is one-way coupled to tau progression.

2) We investigate and demonstrate invertibility and accuracy of estimation for such growth parameters. We perform a sensitivity study with respect to the relative change in tau signal between scans, the effect of tissue atrophy, and the effect of partial observations. Our results indicate good agreement for future prediction of tau uptake compared to the true data.

3) We test our method on clinical tau-PET scans, and study the sensitivity of our model to different subjects, and algorithmic hyper-parameters. To our knowledge, this is the first study of its kind.

Related work. We believe organ-scale biophysical models hold an enormous promise in aiding clinical management of AD. Such models of protein misfolding gained momentum with the advent of the prion-paradigm (misfolding chain-reaction) disease model. Models range from molecular level^{13,14}, to graph models¹⁵⁻¹⁸, and kinetic equations¹⁹. Inspired by the successful application of such models in computational oncology²⁰⁻²³, we use an organ level PDE-model which reflects the most dominant evolution patterns of tau propagation. For AD, a similar model to the one we propose here has been recently proposed for prion-like diseases^{24,25} but did not consider the PET-based calibration problem. To the best of our knowledge, our method is the first one to personalize a biophysical model of tau propagation.

Results

We examine the quality of biophysical model personalization, and the accuracy of subsequent prediction of tau spreading. Specifically, we ask the following two questions: (i) How does the solution of (3) depend on the time horizon T and the effects of tissue atrophy (modeled via material transport)? And (ii) how does our method perform on clinical tau-PET scans? For the latter, we use clinical PET data from the Alzheimer’s Disease Neuroimaging Initiative (ADNI)¹ database.

Synthetic Data. We generate synthetic tau-PET data based on our physics-based model. Fig. 1 gives an illustration of the data and test case setup. As underlying brain anatomy, we use (segmentations of) longitudinal T1 MRI scans of an AD subject with significant tissue atrophy (cf. panel A in Fig. 1). The advection velocity v used to couple the effect of tissue atrophy to tau spreading is obtained from diffeomorphic image registration between segmentations of the T1 MRI. Synthetic tau data is generated using our reaction-diffusion-advection model for tau evolution based on the tissue segmentation of the first time point, and ground truth parameters $\rho^* = 8$, $\kappa = 0.18$, and $v^* = v$ (see panel B in Fig. 1 for an illustration).

Performance Metrics. For our synthetic studies, we report relative errors $\epsilon_\iota = \iota_{rec}/\iota^*$, $\iota \in \{\rho, \kappa\}$ in the reconstruction of the characteristic growth parameters. We further report the relative data misfit $\mu_{\mathcal{O}} = \|\mathcal{O}_T(c_T - d_T)\|_2 / \|d_T\|_2$ of the calibrated model (at observation points defined by \mathcal{O}), as well as the relative forecast errors $\mu_t = \|c(t) - d_t\|_2 / \|d_t\|_2$ for predicted tau concentration at future time points $t \in \{T', T''\}$.

Accuracy of Model Calibration and Tau Forecast

We study the sensitivity of model calibration and prediction to (i) varying time frames of image acquisition, and (ii) the effect of tissue atrophy, one-way coupled via material transport in a synthetic setting, with known ground truth values. For these synthetic tests, we set the observation threshold τ_{obs} to zero (i.e., observe all data). Results are given in Tab. 1. We also study the sensitivity to a nonzero observation threshold in Tab. 2

Sensitivity to Small Relative Change in tau Signal. Tau misfolding, and, hence AD progression is an (initially) slow process. In clinical practice, PET imaging is acquired in intervals of 8 to 15 months with varying, but typically small relative change of measured tau SUV. Hence, we study the sensitivity of the model calibration to smaller relative change in tau uptake. We consider different acquisition times T_0 for the first tau snapshot d_0 , such that the relative change in tau SUV between the two time points varies from 99% to 3%. Tab. 1 (runs #17-#24) shows results for calibration (using the material transport model) and tau forecast. We observe a slight deterioration in reconstruction accuracy of the true model parameters for smaller time horizons between consecutive scans. For particularly small relative change in tau uptake values, we see larger errors and a trend of under-estimating the growth parameters. Up to 10% relative change in tau SUV, relative errors, however, are still small with 5% and below for ρ , and up to 20% for κ . Similarly the accuracy of tau forecast deteriorates marginally, but remains low with errors of 3-13% for T' , and 5-26% for T'' (see also panel C in Fig. 1).

¹<http://adni.loni.usc.edu/>

Table 1. Model calibration and tau evolution forecasting for synthetic data. We study the sensitivity with respect to 1) the time horizon T between consecutive scans, and 2) tissue atrophy (one-way coupled to tau spreading via material transport). For 1), we consider varying image acquisition time points T_0 for d_0 with a relative change (Δ SUV) in tau signal (between scans d_0 and d_1) ranging from 99% to 3%. For 2), we consider three different scenarios: I. Disregard tissue atrophy and use structural MRI of T_0 as material properties for tau-propagation; II. Like before but use MRI of T_1 ; III. Account for tissue atrophy via material transport, governed by a velocity field found from image registration of (segmented) T_1 and T_0 MRI. We report relative errors ϵ_ρ and ϵ_κ for the inversion parameters (true values are $\rho^* = 8$, $\kappa^* = 0.18$). μ_{T_1} denotes the relative data misfit in the inversion; $\mu_{T'}$ and $\mu_{T''}$ denote forecast errors at future times $T' = 1.2$, and $T'' = 1.5$.

ID	T_0	T_1	Δ SUV	ρ	κ	ϵ_ρ	ϵ_κ	μ_{T_1}	$\mu_{T'}$	$\mu_{T''}$	
#1	0.00	1.00	99%	7.77	1.70E-1	2.91E-2	5.34E-2	3.37E-1	3.90E-1	4.42E-1	
#2	0.56	1.00	80%	7.89	1.85E-1	1.37E-2	2.89E-2	3.03E-1	3.70E-1	4.29E-1	
#3	0.72	1.00	60%	7.70	1.52E-1	3.70E-2	1.53E-1	2.56E-1	3.43E-1	4.18E-1	
#4	0.83	1.00	40%	7.21	9.36E-2	9.93E-2	4.80E-1	1.91E-1	3.13E-1	4.17E-1	
#5	0.92	1.00	20%	6.48	4.12E-2	1.90E-1	7.71E-1	1.12E-1	2.80E-1	4.27E-1	
#6	0.96	1.00	10%	5.96	1.49E-2	2.55E-1	9.17E-1	6.03E-2	2.63E-1	4.39E-1	
#7	0.98	1.00	5%	5.78	6.92E-3	2.77E-1	9.62E-1	3.09E-2	2.52E-1	4.43E-1	
#8	0.99	1.00	3%	5.73	4.52E-3	2.84E-1	9.75E-1	1.56E-2	2.45E-1	4.43E-1	
I. T_0 MRI											
#9	0.00	1.00	99%	7.53	1.59E-1	5.93E-2	1.18E-1	2.49E-1	2.66E-1	3.06E-1	
#10	0.56	1.00	80%	7.71	1.65E-1	3.57E-2	8.40E-2	1.84E-1	2.22E-1	2.77E-1	
#11	0.72	1.00	60%	7.70	1.56E-1	3.72E-2	1.36E-1	1.48E-1	2.01E-1	2.67E-1	
#12	0.83	1.00	40%	7.58	1.37E-1	5.19E-2	2.41E-1	1.14E-1	1.83E-1	2.60E-1	
#13	0.92	1.00	20%	7.28	1.07E-1	9.00E-2	4.06E-1	7.35E-2	1.66E-1	2.60E-1	
#14	0.96	1.00	10%	6.83	7.46E-2	1.46E-1	5.86E-1	4.39E-2	1.61E-1	2.75E-1	
#15	0.98	1.00	5%	6.31	4.14E-2	2.12E-1	7.70E-1	2.42E-2	1.69E-1	3.06E-1	
#16	0.99	1.00	3%	6.02	2.36E-2	2.48E-1	8.69E-1	1.26E-2	1.77E-1	3.29E-1	
II. T_1 MRI											
#17	0.00	1.00	99%	7.90	1.80E-1	1.31E-2	4.72E-4	2.38E-2	3.34E-2	5.23E-2	
#18	0.56	1.00	80%	7.90	1.83E-1	1.20E-2	1.71E-2	9.74E-2	1.02E-1	1.11E-1	
#19	0.72	1.00	60%	7.89	1.81E-1	1.37E-2	4.21E-3	9.21E-2	1.09E-1	1.27E-1	
#20	0.83	1.00	40%	7.83	1.72E-1	2.16E-2	4.65E-2	7.30E-2	1.06E-1	1.33E-1	
#21	0.92	1.00	20%	7.70	1.57E-1	3.71E-2	1.25E-1	4.61E-2	9.90E-2	1.38E-1	
#22	0.96	1.00	10%	7.56	1.43E-1	5.45E-2	2.05E-1	2.66E-2	9.42E-2	1.43E-1	
#23	0.98	1.00	5%	6.66	7.22E-2	1.68E-1	5.99E-1	1.76E-2	1.22E-1	2.19E-1	
#24	0.99	1.00	3%	5.97	6.73E-2	2.54E-1	6.26E-1	9.89E-3	1.37E-1	2.64E-1	
III. Adv., T_0 MRI											

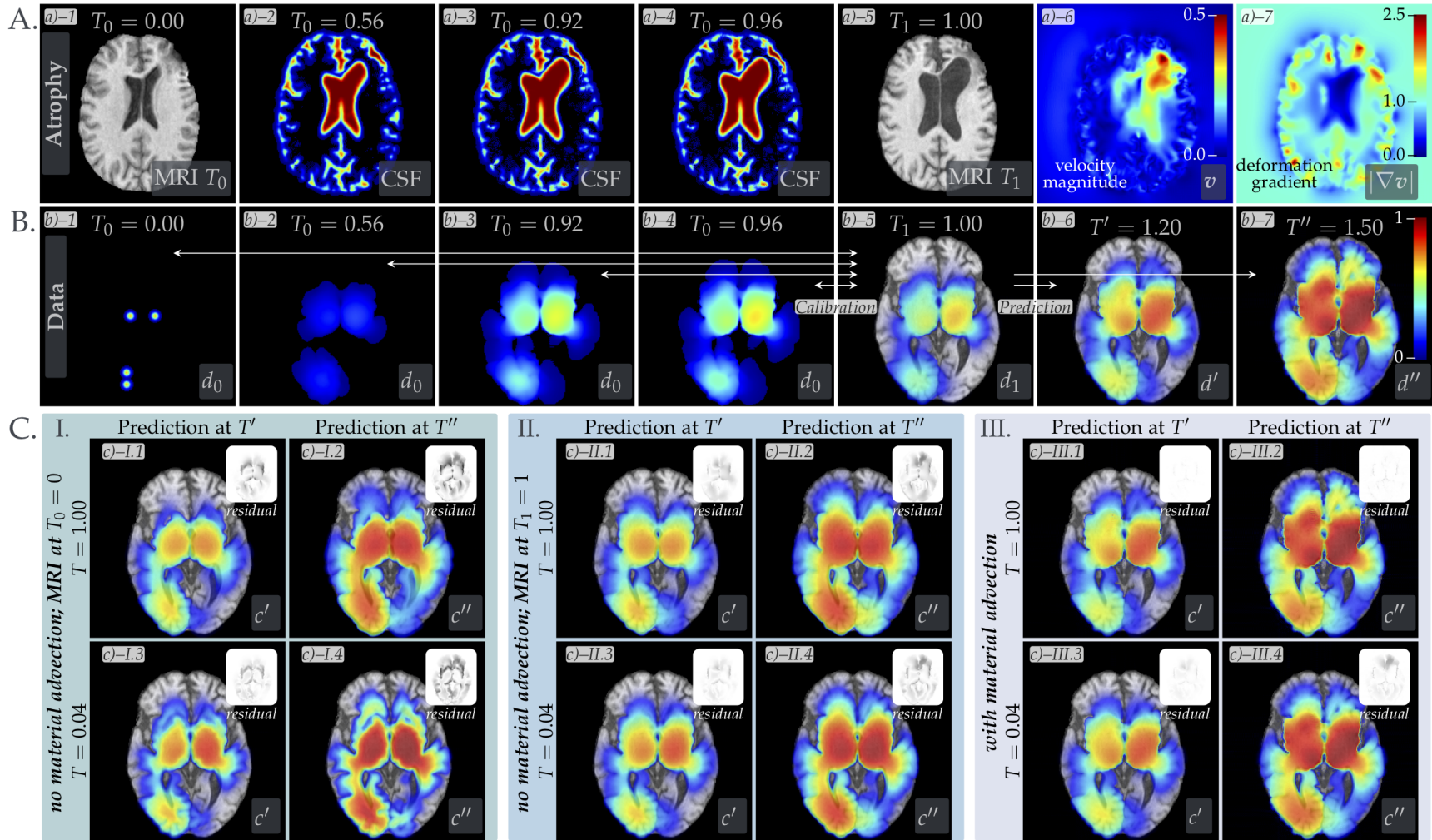


Figure 1. Qualitative results for model calibration and tau evolution forecasting using synthetic data. Panel A illustrates structural differences induced by tissue atrophy: a)-1 and a)-5 show original T1 MRI scans of an AD subject at time points $T_0 = 0$ and $T_1 = 1$; a)-2 through a)-4 show material advection of CSF to account for tissue atrophy at intermediate time points; a)-5 and 6 show the magnitude and deformation gradient of the velocity, obtained from registration of T1 MRI (a value of $|\nabla v| < 1$ indicates contraction, a value above 1 expansion; the registration is performed from the second to the first snapshot). Panel B shows synthetic tau data at different time points used for calibration and tau distribution at forecast time points T' and T'' (cf. Tab. 1). Panel C shows the forecast distribution c' and c'' of tau at time points T' and T'' based on calibration for the three scenarios I-III from Tab. 1 and two different time horizons, along with the relative mismatch to the ground truth (dark black indicates high error).

Sensitivity to Effects from Tissue Atrophy (Material Transport). Next, we study the sensitivity of the model personalization with respect to the material transport, coupling the effects of tissue atrophy to our tau evolution model. For this first study, we consider three scenarios:

- I. Disregard tissue atrophy and use structural MRI of time point T_0 as material properties for tau-propagation;
- II. Like above but use MRI of time point T_1 ;
- III. Account for tissue atrophy via material transport, governed by a velocity field found from image registration of (segmented) MRI.

From Tab. 1 we observe that the effect of tissue atrophy is not negligible for the calibration of our model: Disregarding the material transport which simulates effects of cortical thinning in our model, results in much larger errors for both scenarios I. and II., compared to the full model in scenario III. Most prominently, smaller relative change of tau SUV between scans results in a rapid and more drastic decline of accuracy for both the calibrated growth parameters and the forecast of tau concentration, if the advection of material properties, according to the cortical thinning, is disregarded. The differences in forecast of tau distribution at future time points can be seen from Fig. 1 (panel C) for the different scenarios. We conclude that the proposed model is sensitive to the transport of material properties, and the coupling of tissue atrophy to tau spreading is not negligible for model calibration.

Sensitivity to Partial Observations. We also study the sensitivity of the calibration step to partial observations, meaning that the (synthetic) tau data d_0 and d_T is observed only up to 10%, 20%, 30% and 40% of its maximum concentration. The calibration and forecast results are given in Tab. 2. We observe a strong sensitivity of our model on the threshold of the observation operator, paired with large errors for the parameter reconstruction and tau forecast for higher thresholds. Furthermore, the error is pronounced if the relative change of tau SUV between scans becomes small.

From this first exploratory study using synthetic data, we find that small relative changes of tau SUV between scans as well as partial observations severely complicate the calibration problem. The solution of the latter is further hampered by the noise typically present in actual clinical tau-PET imaging. The presence of noise calls for partial observations to focus attention to informative regions with change of tau SUV, and, consequently require careful calibration of the observation threshold parameter.

Application to Clinical Data

We report reconstruction results in Tab. 3 and Figs. 2 and 2. PET scans are acquired 1-2 years apart; the number of days between image acquisition is given by T . Not all cases have T1 MRI for the second time point; we do not account for atrophy changes for these subjects.

Discussion

Perhaps the most interesting result in our study is that the estimated growth parameters show significant variability across the different subjects. For example, we obtain values for ρ between 2 and 7, and κ ranges between $1.70E-1$ and $1E-4$. This demonstrates that our model is sensitive to patient-specific information and provides an indication that the methodology could be clinically useful for differential diagnosis. Our model is minimal. Despite having only two parameters, the model can reconstruct clinical scans quite accurately. The reconstructed parameters κ and ρ could be used as biomarkers. Finally, the model can be run forward in time to predict tau propagation and estimate AD progression, which can serve as an overall validation. Indeed, having more than two scans would allow us to validate our model by using the first two scans to calibrate and the third scan to test the prediction. This task is our first priority.

Second, the choice of the observation threshold τ_{obs} is critical, and strongly affects the calibration and prediction result. We study the calibration result for three different choices of τ_{obs} . Figs. 2 and ?? show normalized PET scans for two subjects with indicated observation contours in black for various values of τ_{obs} (panels a)–b)). For lower values of τ_{obs} , larger regions of the tau scans are observed. This limits the flexibility of the model to account for localized regional SUV variations (cf. localized intensity changes in tau-PET, panels a)–b) in Figs. 2 and ??). As a result, the estimated proliferative parameter ρ decreases, and the diffusive parameter κ increases, for smaller values of τ_{obs} . Finding an optimal choice for the hyper parameter τ_{obs} requires calibration to a large patient cohort.

For this first exploratory study, we opted for a simple model that captures the dynamics of tau propagation and allows us to establish a calibration baseline upon which more complex models can be evaluated

Table 2. Sensitivity to Observation Threshold. We study the sensitivity with respect to the observation threshold τ_{obs} . Synthetic data d_0 and d_T is observed only up to 10%, 20%, 30% and 40% of the maximum tau concentration, when calibrating the model (compare rows 1–3 in figure; the red contour line indicates the observation threshold). We report relative errors ϵ_ρ and ϵ_κ for the inversion parameters (true values are $\rho^* = 8$, $\kappa^* = 0.18$), the calibration error μ_O at observation points, and forecast errors $\mu_{T'}$ and $\mu_{T''}$. We consider two different time horizons with 80% and 20% relative change in tau SUV, respectively. The last two rows of the figure show c' tau concentrations at forecast time point T' , and corresponding residual.

ID	Δ SUV	τ_{obs}	ρ	κ	ϵ_ρ	ϵ_κ	μ_O	$\mu_{T'}$	$\mu_{T''}$
#25	80%	0.0	7.90	1.83E-1	1.20E-2	1.71E-2	9.74E-2	1.02E-1	1.11E-1
#26	80%	0.1	8.47	2.35E-1	5.87E-2	3.03E-1	9.42E-2	2.59E-1	5.06E-1
#27	80%	0.2	8.98	2.49E-1	1.22E-1	3.84E-1	8.38E-2	3.91E-1	6.33E-1
#28	80%	0.3	9.54	2.90E-1	1.92E-1	6.11E-1	7.53E-2	5.04E-1	7.19E-1
#29	80%	0.4	9.78	2.62E-1	2.23E-1	4.53E-1	6.65E-2	6.07E-1	7.87E-1
#30	80%	0.5	10.76	2.79E-1	3.45E-1	5.52E-1	6.70E-2	7.07E-1	8.47E-1
#31	20%	0.0	7.70	1.57E-1	3.71E-2	1.25E-1	4.61E-2	9.90E-2	1.38E-1
#32	20%	0.1	9.14	2.28E-1	1.43E-1	2.67E-1	6.97E-2	2.64E-1	5.09E-1
#33	20%	0.2	11.78	3.97E-1	4.73E-1	1.21E0	9.36E-2	4.00E-1	6.39E-1
#34	20%	0.3	12.52	1.93E-1	5.65E-1	7.41E-2	7.38E-2	5.28E-1	7.26E-1
#35	20%	0.4	13.09	3.74E-1	6.37E-1	1.08E0	1.28E-1	6.12E-1	7.89E-1
#36	20%	0.5	6.11	5.63E-2	2.36E-1	6.87E-1	1.60E-1	7.13E-1	8.49E-1

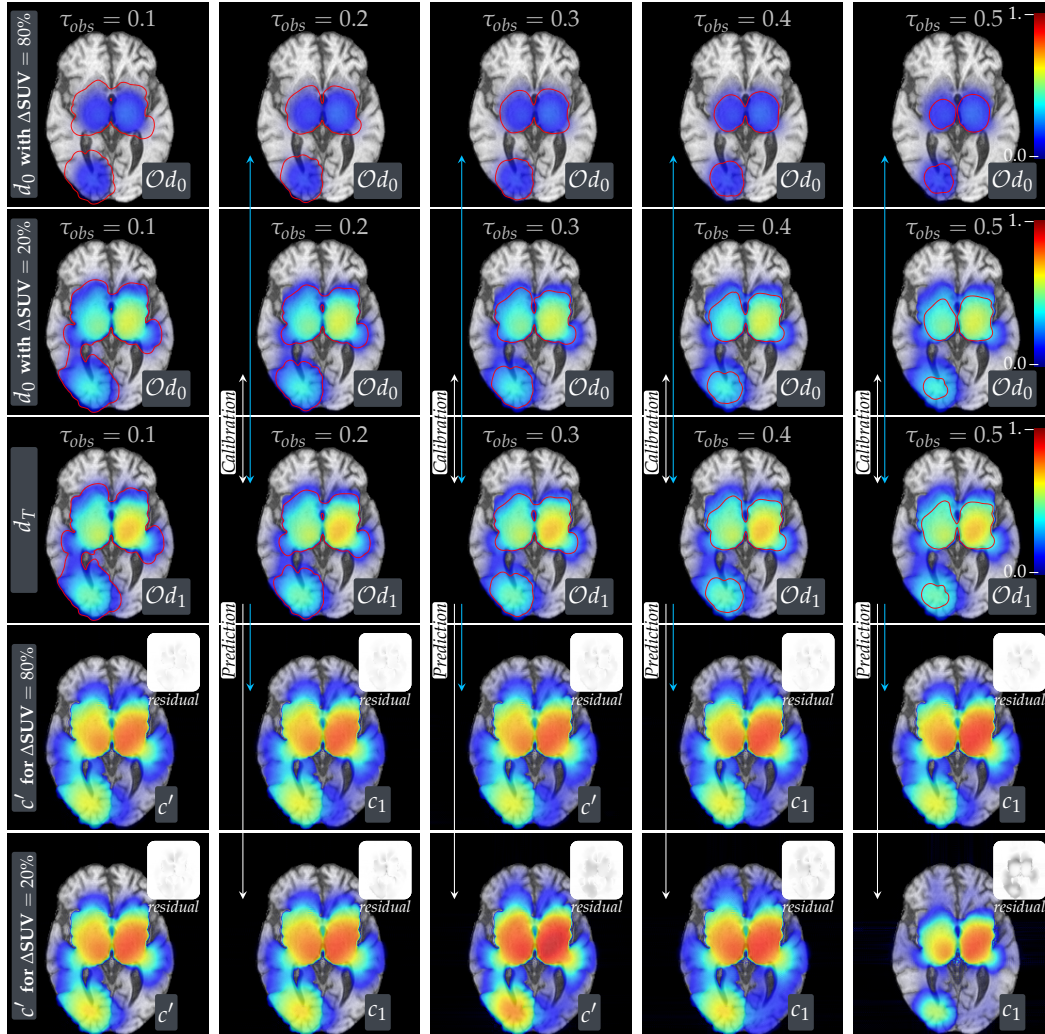
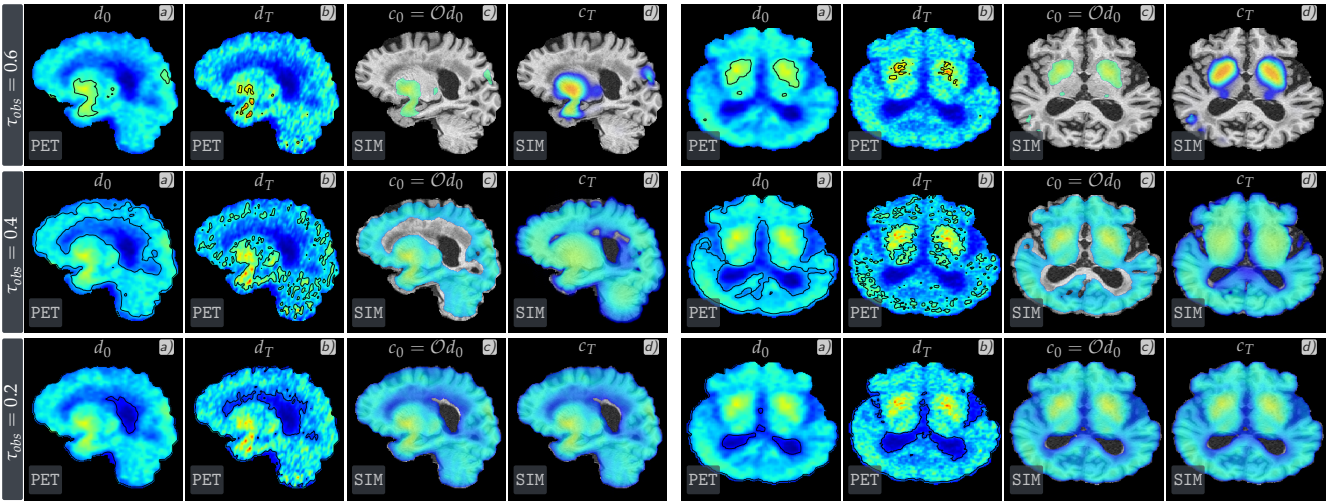


Table 3. Model Personalization for Clinical Data. We report the calibrated growth parameters ρ and κ for seven AD patients, taken from the ADNI database. We investigate sensitivity to the threshold τ_{obs} in the observation operator and consider three different values $\tau_{obs} \in \{0.6, 0.4, 0.2\}$. The time T between scans is given in days. If available, we register T1 MRIs of longitudinal snapshot, and account for atrophy (via material advection) in the personalization step (indicated by “Adv”). For each applied threshold value, we report the relative mismatch $\mu_{\mathcal{O}}$ at observation points, as well as the relative error μ in the entire brain.

Subject ID	T [d]	Adv	Observation Threshold $\tau_{obs} = 0.6$				Observation Threshold $\tau_{obs} = 0.4$				Observation Threshold $\tau_{obs} = 0.2$			
			ρ	κ	μ	$\mu_{\mathcal{O}}$	ρ	κ	μ	$\mu_{\mathcal{O}}$	ρ	κ	μ	$\mu_{\mathcal{O}}$
022_S_6013	401	yes	3.98	3.84E-2	8.30E-1	1.62E-1	1.01	2.35E-1	2.40E-1	1.36E-1	0.10	1.00E-4	1.36E-1	1.21E-1
023_S_1190	476	yes	4.16	4.47E-2	8.76E-1	3.75E-1	1.57	2.15E-1	3.44E-1	2.21E-1	0.57	2.50E-1	2.95E-1	2.33E-1
127_S_4301	477	no	4.00	1.88E-4	9.90E-1	3.53E-1	2.90	5.68E-3	9.66E-1	3.09E-1	1.34	1.89E-1	3.59E-1	2.26E-1
127_S_2234	660	no	2.94	1.74E-1	4.68E-1	2.40E-1	0.60	2.79E-1	2.87E-1	1.65E-1	0.23	2.97E-1	2.89E-1	2.06E-1
035_S_4114	426	yes	6.93	3.70E-2	9.08E-1	3.27E-1	2.96	1.46E-1	4.06E-1	2.63E-1	1.09	1.96E-1	2.96E-1	2.63E-1
033_S_4179	376	no	4.02	2.36E-2	9.26E-1	2.74E-1	2.46	1.86E-1	3.03E-1	1.83E-1	0.00	1.30E-3	1.96E-1	1.69E-1
941_S_4036	464	yes	3.54	1.27E-1	4.06E-1	2.07E-1	0.68	2.70E-1	2.34E-1	1.57E-1	0.00	9.04E-3	1.58E-1	1.41E-1

Subject 035_S_4114



Subject 033_S_4179

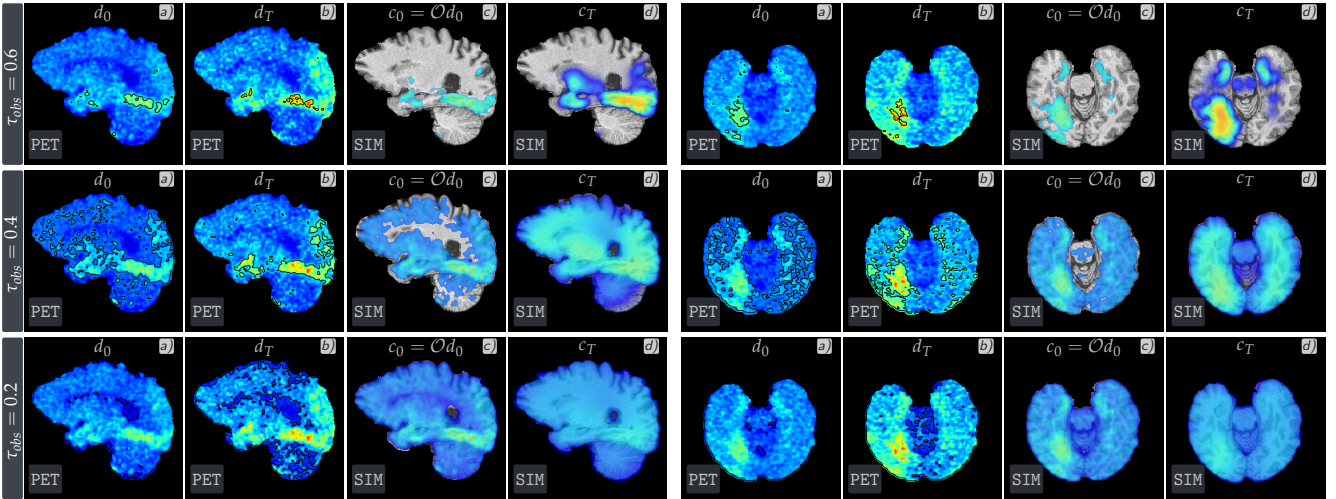


Figure 2. Model Personalization for Clinical Data, ADNI subjects 035_S_4114 and 033_S_4179. The three rows correspond to different observation thresholds $\tau_{obs} = 0.6$ (first row), $\tau_{obs} = 0.4$ (second row), and $\tau_{obs} = 0.2$ (third row). Shown are sagittal and axial cuts of PET data and reconstruction. Panels a) and b) show the normalized PET for both snapshots; the observation threshold is indicated by black contour lines. Panels c) and d) show the initial seeding and predicted tau concentration, overlaid with the T1 MRI.

Limitations and Future Directions. More complex models could be used for tau propagation. An important (and relatively easy to implement) model improvement is to include anisotropic diffusion, especially for data with longer time horizon T . Also in our model, the atrophy is computed from image registration and it is only one-way coupled to tau. In our future work, we will evaluate such models^{6,24}. We remark that more complex models also require more informative data; either more time snapshots of tau or larger time intervals between scans.

Another challenge is the normalization of longitudinal tau PET, especially for longitudinal studies where relative change is small. The choice for a good reference region is not trivial, depends on the employed PET tracer, and is sensitive to, e.g., registration errors²⁶. PET normalization is ongoing research^{27,28}. Other challenges are linked to lack of standardization in PET image acquisition protocols and subsequent normalization. Inconsistent intensity changes, can be caused by several bio-physical factors such as age, weight change, and blood glucose level of the patient; or by other imaging factors such as varying scanner models or image reconstruction algorithms²⁹. Dealing with such challenges would require cross-validation of our method with several subjects in order to select the hyper-parameters in our scheme.

Methods

Models and Materials

Forward Model. To model the spatiotemporal evolution of misfolded tau-protein, we adopt the Fisher-Kolmogorov equation³⁰ coupled with an advection equation for material transport:

$$\partial_t c + \nabla \cdot (c\mathbf{v}) - \kappa \mathcal{D}c - \rho \mathcal{R}c = 0, \quad \text{in } \Omega_B \times (0, T], \quad (1a)$$

$$c(0) = c_0 \quad \text{in } \Omega_B, \quad (1b)$$

$$\partial_t \mathbf{m} + \nabla \mathbf{m} \mathbf{v} = \mathbf{0}, \quad \text{in } \Omega \times (0, T], \quad (1c)$$

$$\mathbf{m}(0) = \mathbf{m}_0 \quad \text{in } \Omega. \quad (1d)$$

This simple model captures the basic dynamics of the problem: (i) The growth and formation of tau aggregates, and (ii) their subsequent fragmentation and spatial propagation. It further represents AD specific characteristics such as slow early stage progression with a rapid acceleration after symptom onset, and the inevitable progression of the disease: even a single corruptive protein will spread, and ultimately cause disease³¹.

Our model follows^{24,25}, but differs in a new image-driven transport term, that captures atrophy without a mechanical model. In our case $c = c(\mathbf{x}, t) \in [0, 1]$ is the tau concentration with initial seeding c_0 . Its evolution over time $t \in [0, T]$ in the three-dimensional brain domain $\Omega_B \subset \Omega = [0, 2\pi]^3$ is governed by the coefficients of the reaction and diffusion terms in (1a): The nonlinearity $\mathcal{R}c = \rho_m c(1 - c)$ with growth rate ρ provides a saturation term expressing the maximal concentration of toxic proteins. ρ_m is a spatially variable coefficient, dependet on the underlying material properties $\mathbf{m} = (m_i(\mathbf{x}, t))_{i=W,G,F}$, a vector of voxelwise probabilities for *white matter* (W), *gray matter* (G), and *cerebrospinal fluid with ventricles* (F). Spatial spreading of tau is driven by *extracellular diffusion* and *axonal transport*. This is modeled by the diffusion operator $\mathcal{D}c = \nabla \cdot \kappa_m \nabla c$, where $\kappa_m = \kappa_0 \mathbf{I} + (\kappa_i/\kappa - 1)\mathbf{T}$ defines the inhomogeneous (anisotropic) diffusion tensor. κ_0 captures the inhomogeneous diffusion based on the material properties \mathbf{m} , while \mathbf{T} expresses preferential direction of diffusion along the axon bundle weighted by κ_i , and enables anisotropy. Tau does not invade the cerebrospinal fluid, and spreading occurs primarily in white matter³².

We approximate no-flux boundary conditions $\partial\Omega_B$ via a penalty approach³³, and use periodic boundary conditions on $\partial\Omega$.

Atrophy: Advection of Material Properties. Over time, tau aggregates disrupt cell function and ultimately cause cell death and tissue atrophy (thinning of white and gray matter)⁶. We model tissue atrophy as image-driven transport equation (1c)–(1d) of the spatiotemporal material properties \mathbf{m} . As a result, tissue atrophy is one-way coupled to tau spreading via the definition of the spatially variable diffusion and reaction coefficients.

The velocity field \mathbf{v} is found via large-deformation diffeomorphic image registration of longitudinal MRI data, and can be computed solving the inverse problem

$$\min_{\mathbf{v}} \frac{1}{2} \|\vec{m}(1) - \vec{m}_T\|_{L^2(\Omega)}^2 + \frac{\beta}{2} \mathcal{S}(\mathbf{v}) \quad \text{s.t. (1c)–(1d)}. \quad (2)$$

Here, \vec{m}_0 and \vec{m}_T denote segmentations of T1 MRI, corresponding to the acquisition times $t = 0$ and $t = T$ of the tau-PET time-series. The regularization term $\mathcal{S}(\mathbf{v})$ is given as an H^1 -seminorm $\int_{\Omega} \sum_{i=1}^3 |\nabla v^i(\mathbf{x})|^2 dx$. For the solution of (2) we use the registration software `CLAIRE`³⁴. The proposed atrophy model is distinct from other

approaches in the literature. In^{24,25} the authors couple a reaction-diffusion equation to a mechanical deformation model for atrophy, based on nonlinear elasticity.

Solving (1) defines the *forward problem* $\mathcal{F}(c_0, c_T, \vec{v}, \rho, \kappa) = 0$. Next, we discuss the image-driven calibration of this model.

Model Calibration and Extraction of Tau-Spreading Characteristics

The model is personalized based on patient specific, tau-PET imaging data. That is, we estimate biophysical growth parameters $\mathbf{g} = (\rho, \kappa)$ in (1) based on measurements of tau uptake value ratios (SUVR) from longitudinal PET by solving a *parameter estimation problem*

$$\min_{\mathbf{g}=(\rho,\kappa)} \frac{1}{2} \|\mathcal{O}_T(c_T - d_T)\|_{L^2(\Omega)}^2 \quad \text{s.t. } \mathcal{F}(c_0, c_T, \vec{v}, \rho, \kappa) = 0, \quad \text{from (1)}, \quad (3)$$

minimizing the discrepancy between predicted tau concentration $c_T = c(T)$ (based on the seeding $c(0)$) and the target data d_T . The *observation operator* \mathcal{O}_i is defined as $\mathcal{O}_i c := \mathbb{1}[d_i(\mathbf{x}) > \varepsilon]c$ with threshold $\varepsilon = \tau_{obs} \cdot \max(d_i)$ for $i = 0, T$. In other words, points with uptake values below τ_{obs} percent of the maximum concentration of d_0 and d_T , respectively, are not observed. This is critical due to the low signal-to-noise ratio in PET imaging. Observation in the entire brain would disregard localized relative changes of SUVR, and drive the growth parameters close to zero. The seeding concentration $c(0)$ is given by the observation points of the data d_0 from the first time point $\mathcal{O}_0 d_0 =: c_0$. As a proof of concept, we only consider isotropic diffusion for the model calibration. The extension to anisotropy is straightforward and will be realized in future work. Next, we discuss the numerical scheme for the solution of (3).

Numerical Scheme

Numerical Solution of the Forward Problem. We employ a pseudo-spectral Fourier approach on a regular grid for spatial discretization. That means all spatial differential operators are computed via a 3D fast Fourier Transform³⁵. For numerical solution of the forward problem, we employ a first-order operator-splitting method to split the tau progression equation (1a) into a reaction, diffusion, and advection part. For the diffusion split, we use an implicit Crank-Nicholson method, and solve the linear system with a preconditioned matrix-free CG method. The reaction sub-steps are solved analytically. The *hyperbolic transport equations* are solved using an unconditionally stable semi-Lagrangian time-stepping scheme to avoid stability issues and small, CFL restricted time-steps^{2,36,37}. This method requires evaluations of the space-time fields at off-grid locations, defined by the characteristic associated with \mathbf{v} . We compute off-grid evaluations using a cubic Lagrange polynomial interpolation model. We use $n_t = 100$ time steps of size $\Delta t = 0.01$ for the time integration.

Numerical Optimization. The optimization problem (3) is solved using a bound constrained, limited memory BFGS quasi-Newton solver globalized with Armijo line-search. The gradient is computed using a first-order accurate finite difference scheme with $\vec{h} = \sqrt{\varepsilon_{mach}} \vec{g}$, for $\vec{g} = (\rho, \kappa)^T$. We terminate the optimization after a gradient reduction of 4 orders of magnitude (relative to the initial guess). To keep the optimizer within feasible bounds, and prevent bad local minima, we define bound constraints $\kappa_{min} = 1\text{E}-4$, and $\kappa_{max} = 1$, $\rho_{min} = 0.1$, and $\rho_{max} = 15$.²

Workflow Summary

For the evaluation on clinical data, we use seven AD subjects from the ADNI database as outlined in Tab. 3. Imaging data is processed using FSL³⁸ by applying the following steps: (i) longitudinal T1 MRI are rigidly registered to the first time point using FLIRT³⁹; (ii) longitudinal tau-PET images are rigidly registered to the first time point T1 MRI; (iii) aligned T1 images are skull-stripped using BET⁴⁰; (iv) registered T1 brain masks are applied in PET space to obtain the skull-stripped PET image; (v) skull-stripped T1 images are segmented using FAST⁴¹; (vi) PET images are individually normalized with average tau uptake value in the cerebellum. For the last step, the cerebellum is extracted from a registered labeled standard template.

References

1. Jucker, M. & Walker, L. C. Self-propagation of pathogenic protein aggregates in neurodegenerative diseases. *Nature* **501**, 45–51 (2013).

²The lower bound for κ_i is determined by the smallest recoverable diffusivity considering a resolution of 256^3 .

2. Walker, L. C. & Jucker, M. Seeds of dementia. *Sci. Am.* **308**, 52–57 (2013).
3. Jucker, M. & Walker, L. C. Propagation and spread of pathogenic protein assemblies in neurodegenerative diseases. *Nat. Neurosci.* **21**, 1341–1349 (2018).
4. Brettschneider, J., Tredici, K. D., Lee, V. M. Y. & Trojanowski, J. Q. Spreading of pathology in neurodegenerative diseases: a focus on human studies. *Nat. Rev. Neurosci.* **16**, 109–120 (2015).
5. Ossenkoppele, R. *et al.* Tau pet patterns mirror clinical and neuroanatomical variability in alzheimer’s disease. *Brain* **139**, 1551–1567 (2016).
6. La Joie, R. *et al.* Prospective longitudinal atrophy in alzheimer’s disease correlates with the intensity and topography of baseline tau-pet. *Sci. Transl. Medicine* **12** (2020).
7. Rowe, C. C. & Villemagne, V. L. Amyloid imaging with pet in early alzheimer disease diagnosis. *Med. Clin.* **97**, 377–398 (2013).
8. Jucker, M. & Walker, L. C. Pathogenic protein seeding in alzheimer disease and other neurodegenerative disorders. *Annals neurology* **70**, 532–540 (2011).
9. James, O. G., Doraiswamy, P. M. & Borges-Neto, S. Pet imaging of tau pathology in alzheimer’s disease and tauopathies. *Front. neurology* **6**, 38 (2015).
10. Lowe, V. J. *et al.* An autoradiographic evaluation of av-1451 tau pet in dementia. *Acta neuropathologica communications* **4**, 58 (2016).
11. Smith, R. *et al.* 18f-av-1451 tau pet imaging correlates strongly with tau neuropathology in mapt mutation carriers. *Brain* **139**, 2372–2379 (2016).
12. Schöll, M. *et al.* Distinct 18f-av-1451 tau pet retention patterns in early-and late-onset alzheimer’s disease. *Brain* **140**, 2286–2294 (2017).
13. Cohen, F. *et al.* Structural clues to prion replication. *Science* **264**, 530–531 (1994).
14. Jarrett, J. T. & Lansbury, P. T. Seeding “one-dimensional crystallization” of amyloid: A pathogenic mechanism in alzheimer’s disease and scrapie? *Cell* **73**, 1055 – 1058 (1993).
15. Abdelnour, F., Voss, H. U. & Raj, A. Network diffusion accurately models the relationship between structural and functional brain connectivity networks. *NeuroImage* **90**, 335 – 347 (2014).
16. Raj, A., Kuceyeski, A. & Weiner, M. A network diffusion model of disease progression in dementia. *Neuron* **73**, 1204–1215 (2012).
17. Iturria-Medina, Y. *et al.* Multifactorial causal model of brain (dis) organization and therapeutic intervention: application to alzheimer’s disease. *Neuroimage* **152**, 60–77 (2017).
18. Davis, J. K. & Sindi, S. S. A study in nucleated polymerization models of protein aggregation. *Appl. mathematics letters* **40**, 97–101 (2015).
19. Bertsch, M., Franchi, B., Marcello, N., Tesi, M. C. & Tosin, A. Alzheimer’s disease: a mathematical model for onset and progression. *Math. Medicine Biol. A J. IMA* **34**, 193–214 (2016).
20. Yankeelov, T. *et al.* Clinically relevant modeling of tumor growth and treatment response. *Sci. translational medicine* **5**, 187ps9–187ps9 (2013).
21. Alfonso, J. *et al.* The biology and mathematical modelling of glioma invasion: a review. *J. Royal Soc. Interface* **14**, 20170490 (2017).
22. Hoguea, C., Davatzikos, C. & Biros, G. An image-driven parameter estimation problem for a reaction-diffusion glioma growth model with mass effects. *J. Math. Biol.* **56**, 793–825 (2008).
23. Lipková, J. *et al.* Personalized radiotherapy design for glioblastoma: Integrating mathematical tumor models, multimodal scans, and bayesian inference. *IEEE Transactions on Med. Imaging* **38**, 1875–1884 (2019).
24. Weickenmeier, J., Kuhl, E. & Goriely, A. Multiphysics of prionlike diseases: Progression and atrophy. *Phys. review letters* **121**, 158101 (2018).
25. Weickenmeier, J., Jucker, M., Goriely, A. & Kuhl, E. A physics-based model explains the prion-like features of neurodegeneration in alzheimer’s disease, parkinson’s disease, and amyotrophic lateral sclerosis. *J. Mech. Phys. Solids* **124**, 264–281 (2019).

26. Landau, S. M. Optimizing longitudinal amyloid- β pet measurement: the challenges of intensity normalization. *J. Nucl. Medicine* **59**, 1581–1582 (2018).
27. Rajagopalan, V. & Pioro, E. P. Longitudinal 18f-fdg pet and mri reveal evolving imaging pathology that corresponds to disease progression in a patient with als-ftd. *Front. neurology* **10** (2019).
28. Jack Jr, C. R. *et al.* Longitudinal tau pet in ageing and alzheimer’s disease. *Brain* **141**, 1517–1528 (2018).
29. Boellaard, R. *et al.* Standards for pet image acquisition and quantitative data analysis. *J Nucl Med* **50**, 11S–20S (2009).
30. Murray, J. D. *Mathematical biology* (Springer, New York, 1989).
31. Masel, J., Jansen, V. A. & Nowak, M. A. Quantifying the kinetic parameters of prion replication. *Biophys. Chem.* **77**, 139 – 152 (1999).
32. Iaccarino, L. *et al.* Local and distant relationships between amyloid, tau and neurodegeneration in alzheimer’s disease. *NeuroImage: Clin.* **17**, 452–464 (2018).
33. Gholami, A., Mang, A. & Biros, G. An inverse problem formulation for parameter estimation of a reaction-diffusion model of low grade gliomas. *J. Math. Biol.* **72**, 409–433 (2016).
34. Mang, A., Gholami, A., Davatzikos, C. & Biros, G. CLAIRE: A distributed-memory solver for constrained large deformation diffeomorphic image registration. *SIAM J. on Sci. Comput.* **41**, C548–C584 (2019).
35. Gholami, A. *et al.* A framework for scalable biophysics-based image analysis. In *Proc ACM/IEEE Conference on Supercomputing*, 19, 19:1–19:13 (2017).
36. Mang, A., Gholami, A. & Biros, G. Distributed-memory large-deformation diffeomorphic 3D image registration. In *Proc ACM/IEEE Conference on Supercomputing* (2016).
37. Mang, A. & Biros, G. A semi-Lagrangian two-level preconditioned Newton–Krylov solver for constrained diffeomorphic image registration. *SIAM J. on Sci. Comput.* **39**, B1064–B1101 (2017).
38. Jenkinson, M., Beckmann, C. F., Behrens, T. E., Woolrich, M. W. & Smith, S. M. Fsl. *NeuroImage* **62**, 782 – 790 (2012). 20 YEARS OF fMRI.
39. Jenkinson, M. & Smith, S. A global optimisation method for robust affine registration of brain images. *Med. Image Analysis* **5**, 143 – 156 (2001).
40. Jenkinson, M., Pechaud, M., Smith, S. *et al.* Bet2: Mr-based estimation of brain, skull and scalp surfaces. In *Eleventh annual meeting of the organization for human brain mapping*, vol. 17, 167 (Toronto., 2005).
41. Zhang, Y., Brady, M. & Smith, S. Segmentation of brain mr images through a hidden markov random field model and the expectation-maximization algorithm. *IEEE transactions on medical imaging* **20**, 45–57 (2001).